Monthly Notices
of the
ROYAL ASTRONOMICAL SOCIETY

MNRAS **440,** 2901–2915 (2014) doi:10.1093/mnras/stu467

Deep radio observations of the radio halo of the bullet cluster 1E 0657−55.8

Timothy W. Shimwell,[1⋆] Shea Brown,[2] Ilana J. Feain,[1] Luigina Feretti,[3] B. M. Gaensler[4] and Craig Lage[5]

[1]*CSIRO Astronomy & Space Science, Australia Telescope National Facility, PO Box 76, Epping, NSW 1710, Australia*
[2]*Department of Physics and Astronomy, University of Iowa, 203 Van Allen Hall, Iowa City, IA 52242, USA*
[3]*INAF – Istituto di Radioastronomia, via Gobetti 101, I-40129 Bologna, Italy*
[4]*Sydney Institute for Astronomy, School of Physics, The University of Sydney, NSW 2006, Australia*
[5]*Center for Cosmology and Particle Physics, Department of Physics, New York University, New York, NY 10003, USA*

Accepted 2014 March 6. Received 2014 March 5; in original form 2013 October 11

ABSTRACT

We present deep 1.1–3.1 GHz Australia Telescope Compact Array observations of the radio halo of the bullet cluster, 1E 0657−55.8. In comparison to existing images of this radio halo, the detection in our images is at higher significance. The radio halo is as extended as the X-ray emission in the direction of cluster merger but is significantly less extended than the X-ray emission in the perpendicular direction. At low significance, we detect a faint second peak in the radio halo close to the X-ray centroid of the smaller sub-cluster (the bullet) suggesting that, similarly to the X-ray emission, the radio halo may consist of two components. Finally, we find that the distinctive shape of the western edge of the radio halo traces out the X-ray detected bow shock. The radio halo morphology and the lack of strong point-to-point correlations between radio, X-ray and weak-lensing properties suggest that the radio halo is still being formed. The colocation of the X-ray shock with a distinctive radio brightness edge illustrates that the shock is influencing the structure of the radio halo. These observations support the theory that shocks and turbulence influence the formation and evolution of radio halo synchrotron emission.

Key words: acceleration of particles – radiation mechanisms: non-thermal – shock waves – galaxies: clusters: individual: 1E 0657−55.8 – galaxies: clusters: intracluster medium – radio continuum general.

1 INTRODUCTION

Low surface brightness, steep spectrum, diffuse radio emission has been observed to be associated with the intracluster medium (ICM) of many merging galaxy cluster systems (see Ferrari et al. 2008; Brüggen et al. 2012; Feretti et al. 2012 for recent reviews). The emission is due to synchrotron radiation from relativistic electrons gyrating in a magnetic field. When coincident with the centre of the merging cluster system, this emission is referred to as a radio halo, whereas if located on the periphery of the cluster it is known as a radio relic – Kempner et al. (2004) provide details on the classification of extended radio sources in galaxy clusters. While radio haloes are believed to be the result of cluster-wide processes such as post-merger turbulence (see e.g. Brunetti et al. 2001; Petrosian 2001) or proton–proton collisions (see e.g. Dennison 1980), radio relics are believed to be associated in some way with localized, post-merger shock fronts (Ensslin et al. 1998). Measurements of X-ray shocks in the regions of radio relics (see e.g. Macario et al. 2011; Bourdin et al. 2013; Giacintucci et al. 2008; Ogrean et al. 2013; Akamatsu & Kawahara 2013; Ogrean & Brüggen 2013) and synchrotron radio spectral index gradients (see e.g. van Weeren et al. 2010) have provided strong support to the theory that these objects are formed by first-order Fermi acceleration (diffusive shock acceleration). The exact connection/relationship between relics and haloes is unknown, but some observations of radio haloes have shown that weak X-ray shocks are approximately cospatial with edges of radio haloes (see e.g. Brown & Rudnick 2011; Markevitch 2012). An example of such a system is 1E 0657−55.8 (usually referred to as 'the bullet cluster' because of its distinctive morphology). In this case, the radio images of the powerful radio halo indicate that it has an irregular shape (Liang et al. 2000) and that the position of the radio edge and the X-ray shock is similar; however, it was unclear from the halo observations by Liang et al. (2000) whether there was any correspondence between the morphology of the distinctive X-ray bow shock and the (indistinct) radio halo edge. We have obtained observations that are deeper than those of Liang et al. (2000) and are able to characterize the halo in greater detail and at higher resolution. The primary aim of this study is to determine whether shocks influence the structure of radio haloes.

⋆ E-mail: tws29@mrao.cam.ac.uk

The bullet cluster with its prominent bow shock and bright radio halo is an obvious source for investigating the relationship between shocks and radio haloes. We have used the Australia Telescope Compact Array (ATCA) to obtain deep, large fractional bandwidth (1.1–3.1 GHz), polarimetric observations of the bullet cluster which we use to compare the radio emission from relativistic electrons with the X-ray emission from thermal gas.

Hereafter we assume a concordance Λ cold dark matter cosmology, with $\Omega_{\rm m} = 0.3$, $\Omega_\Lambda = 0.7$ and $h \equiv H_0/(100\ {\rm km\ s^{-1}\ Mpc^{-1}}) = 0.7$. At $z = 0.296$, the luminosity distance of 1E 0657−55.8 is 1529 Mpc and 1 arcsec corresponds to 4.413 kpc. All coordinates are given in J2000.

2 OBSERVATIONS

2.1 Archival radio data

Liang et al. (2000) presented a serendipitous discovery of a radio halo associated with 1E 0657−55.8 and using 128 MHz bandwidth ATCA observations centred at 1.3, 2.4, 4.9, 5.9 and 8.8 GHz as well as 843 MHz Molonglo Observatory Synthesis Telescope observations, they characterized its properties. By integrating over a 3.5 Mpc^2 region of the cluster, they measured that the halo has a total flux density of 78 ± 5 mJy at 1.3 GHz. In a central 0.78 Mpc^2 region, where the halo is brightest, they measured an integrated flux density of ≈50 mJy at 1.3 GHz and a 0.8–8.8 GHz spectral index $\alpha = -1.3 \pm 0.1$ (where $I_\nu \propto \nu^\alpha$) with no significant spectral steepening between these frequency limits. Combining the large-area integrated flux measurement and smaller scale spectral index measurement, they calculated the rest-frame 1.4 GHz power of the halo to be $4.3 \pm 0.3 \times 10^{25}$ W Hz^{-1}. The cosmology used by Liang et al. (2000) assumed that 1 arcsec corresponds to 5.45 kpc; with this cosmology 0.78 and 3.5 Mpc^2 correspond to 7.3 and 32.7 arcmin^2, respectively.

Liang et al. (2000) did not detect polarization in the radio halo but derived upper limits of 20, 6.5 and 1.4 per cent at resolutions of 10, 20 and 60 arcsec from 1.3 GHz images. The authors noted the similarity between the X-ray and radio halo surface brightness distributions but added that there appeared to be a tighter correspondence between the halo emission and the optical galaxy distribution.

The thermal noise in the Liang et al. (2000) images at a resolution of 60 arcsec is 1100, 51, 110, 56, 65 and 56 μJy beam^{-1} at frequencies of 0.8, 1.3, 2.4, 4.9, 5.9 and 8.8 GHz, respectively. The 1.3 GHz data were also mapped with resolutions of 6.5 and 23 arcsec; the noise levels on these images were 44 and 90 μJy beam^{-1}, respectively.

2.2 Recent radio data

Since the observations presented by Liang et al. (2000) were performed, the ATCA has undergone a significant upgrade in which the bandwidth, spectral resolution and system temperature have all been improved (see Wilson et al. 2011).

We used the ATCA to observe 1E 0657−55.8 on 2012 December 17 and 22, 2013 January 2, 2013 February 17, and 2014 January 8 and 10 (project C2756). ATCA observations of our target were centred at the coordinates used by Liang et al. (2000) and were interleaved every 30 min with 5 min phase-calibrator observations. For amplitude calibration, PKS B1934−638 was observed for 10 min in each of the observing sessions. We observed in the 1.5B, 1.5D, 6A and 6B configurations to provide a compromise between high surface brightness sensitivity and angular resolution. Long-duration observations in each configuration gave good *uv*-coverage and sensitivity to different angular scales – the measured thermal noise as a function of resolution for our observations of the bullet cluster is shown in Fig. 1. The noise continues to decrease a little beyond the diffraction limit as the sidelobes are suppressed. The shortest baseline with which we have observed is 31 m (corresponding to angular scales of 30.2 arcmin at 1.1 GHz or 10.7 arcmin at 3.1 GHz) and the longest baseline used was 5970 m (corresponding to 9.4 arcsec at 1.1 GHz and 3.3 arcsec at 3.1 GHz). A summary of the observations is provided in Table 1.

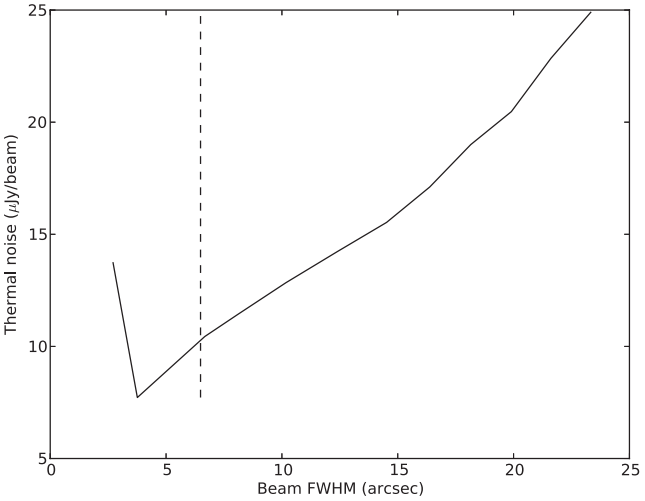

Figure 1. The measured thermal noise of the 1.1–3.1 GHz ATCA observations towards 1E 0657−55.8 as a function of angular resolution. The natural resolution (marked with a dashed vertical line) of our observations is 6.5 arcsec, and at this resolution the sensitivity is 10 μJy beam^{-1}.

Table 1. A summary of our ATCA observations towards 1E 0657−55.8. The quoted synthesized beam FWHM and sensitivity correspond to a natural weighting of the visibilities; however, the data were imaged at a variety of resolutions between 2.7 and 23.3 arcsec. Fig. 1 demonstrates how the sensitivity varies as a function of synthesized beam size for these data. The observations were carried out in four configurations of the ATCA antennas; the target was observed for 8, 5, 9 and 10 h in the 1.5B, 1.5D, 6A and 6B arrays, respectively. The measured polarizations allow for Stokes *I*, *Q*, *U* and *V* imaging.

Coordinates (J2000)	06:58:32.7 −55:57:19.0
Amplitude calibrator	PKS B1934−638
Phase calibrator	PMN J0742−56
Receiver noise	14 μJy beam^{-1}
On-source time	32 h
Frequency range	1.1–3.1 GHz
Spectral resolution	1 MHz
Synthesized beam FWHM	6.5 arcsec natural resolution
Primary beam FWHM	42–15 arcmin
Polarizations measured	XX, YY, XY and YX

3 DATA REDUCTION

3.1 Calibration

The data from the target, amplitude calibrator and phase calibrator were excised of data from bad channels and radio frequency interference using the MIRIAD implementation of AOFlagger (Offringa et al. 2010) and additional manual flagging. The remaining data

were then calibrated using MIRIAD[1] (Sault, Teuben & Wright 1995). The stable calibrator source, PKS B1934−638, which has no linear or circular polarization and a flux density as a function of frequency as characterized by Reynolds (1994), was used to perform a calibration of the complex gains across the bandpass and to determine the polarization leakages. The phase calibrator, PMN J0742−56, was used to refine calibration parameters and to update those that vary with time.

The Stokes *I* data were further calibrated in MIRIAD with four iterations of phase self-calibration followed by a single iteration of phase-plus-amplitude self-calibration. This procedure requires an accurate CLEAN component model, which was created by multi-frequency CLEANing the Stokes *I* data with visibilities weighted such that the synthesized beam size was 4 arcsec. The CLEAN component model was built up slowly through the multiple imaging iterations. Initially, the model contained only the most significant CLEAN components, but after the full number of iterations CLEAN components from regions in which the flux density exceeded five and three times the thermal noise were used for the phase self-calibration and phase-plus-amplitude self-calibration, respectively.

3.2 Continuum imaging

After self-calibration in MIRIAD, the data were imaged in CASA[2] using the multi-scale multi-frequency deconvolution algorithm (Rau & Cornwell 2011) to accurately map the complex and extended structure of the 1E 0657−55.8 radio halo and surrounding region. The images were CLEANed to five times the thermal noise with deconvolution scale sizes equal to zero (point source), one and three times the synthesized beam. This procedure was performed to create full bandwidth (1.1–3.1 GHz) Stokes *I* images.

The 1E 0657−55.8 radio halo has a linear angular extent of >4 arcmin and the data were imaged with various visibility weightings to examine how its observed structure changes as the synthesized beam full width at half-maximum (FWHM) is varied from 2.7 to 23.3 arcsec. The robust parameter within the Briggs (1995) weighting scheme was used to apply a more uniform weighting to visibilities across the *uv*-plane, and a Gaussian taper was applied to reduce the weight of the data from the long baselines. Fig. 1 shows the measured sensitivity as a function of synthesized beam area and Fig. 2 shows a medium resolution 1.1–3.1 GHz image of the data set.

3.3 Radio source detection and subtraction

To study the faint diffuse emission from the radio halo, it is vital that contaminating sources are identified and removed from the data. To isolate such sources from the radio halo, we imaged the data from baselines longer than 4000λ at high resolution (FWHM = 2.7 arcsec) to resolve out the extended radio halo and used the SOURCEFIND software package (AMI Consortium: Franzen et al. 2011) to detect sources with flux densities greater than 5σ in this image, where σ varies across the map due to confusion noise and noisy regions around bright sources (see AMI Consortium: Shimwell et al. 2013).

We identified a total of 57 sources within 6 arcmin (at $z = 0.296$ this corresponds to 1.59 Mpc) of the pointing centre, and of these 43 are extended, where we define sources as extended whose area exceeds 1.4 times the area of the synthesized beam. Fourteen sources lie within the halo (see Table 2 and Fig. 3), and the CASA tasks *ft* and *uvsub* were used to subtract the CLEAN components of these contaminating sources from the visibilities. Unfortunately, residuals remain on the images after subtraction (see Table 2), and although these residuals are small, they contaminate our images of the halo. Therefore, on all source subtracted images, we mark the positions of subtracted sources, so that the reader can treat these areas with caution.

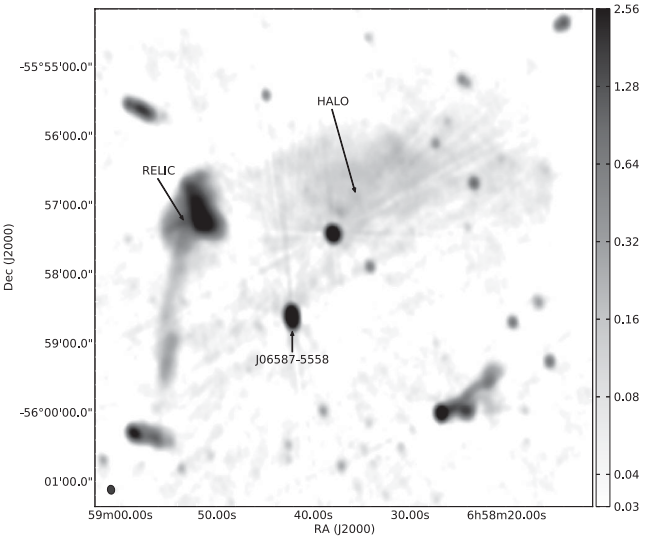

Figure 2. A primary beam corrected, medium-resolution (synthesized beam FWHM ≈ 7 arcsec), Stokes *I*, 1.1–3.1 GHz image towards 1E 0657−55.8. The grey-scale is in mJy beam^{-1} and the measured thermal noise is 11 μJy beam^{-1}. The radio halo, LEH2001 J06587−5558 and the proposed radio relic are labelled.

3.4 Spectral index measurements

We derived spectral index measurements using the following two methods.

(1) *Wide-band method*: multi-scale multi-frequency CLEAN was used to image the entire 1.1–3.1 GHz band using two Taylor terms to describe the sky brightness as a function of frequency

(2) *Narrow-band method*: the 1.1–3.1 GHz band was split into 290 MHz sub-bands, and multi-scale multi-frequency CLEANing was applied to each sub-band image separately.

The first approach makes better use of the data; due to the more complete *uv*-coverage, deconvolution using all 1.1–3.1 GHz channels will be more reliable than that obtained in any single 290 MHz sub-band. However, images with such a large fractional bandwidth are not frequent in the literature and thus we also use the narrow-band method, a more traditional spectral index imaging technique, to reassure readers that the wide-band method is valid for these data. We created spectral index images with different resolutions by weighting the visibilities appropriately (see Section 3.2).

3.4.1 Wide-band method

The multi-frequency imaging that we described in Section 3.2 was performed with two Taylor polynomial terms to describe the sky brightness as a function of frequency,

$$I_\nu = I_0 + I_1 \left(\frac{\nu - \nu_0}{\nu_0} \right), \quad (1)$$

[1] http://www.atnf.csiro.au/computing/software/miriad/
[2] http://casa.nrao.edu/

Table 2. Parameters of the 14 radio sources with flux densities exceeding 5σ, which contaminate the 1.1–3.1 GHz emission from the radio halo. The wide-band flux measurements were obtained from the 2.7 arcsec resolution primary beam corrected 1.1–3.1 GHz image shown in Fig. 3. The sources have been subtracted from the wide-band data following the procedure described in Section 3.3, and the residual contamination after subtraction is given in this table. Images of the 1.1–3.1 GHz data before CLEAN component subtraction are shown in Figs 2 and 3, and images after CLEAN component subtraction are shown in Figs 5 and 6. For sources detectable in 290 MHz sub-bands (see Section 3.4.2), we have derived spectral index parameters and 2.1 GHz flux-density measurements from narrow-band primary beam corrected images that have been convolved to all having an equal resolution of 6.9 arcsec.

Source ID	Right ascension	Declination	1.1–3.1 GHz peak flux density (mJy)	1.1–3.1 GHz integrated flux density (mJy)	Extended at 2.7 arcsec resolution	Residual 1.1–3.1 GHz flux density (μJy)	$\alpha_{1.1}^{3.1}$	2.1 GHz peak flux density (mJy)	2.1 GHz integrated flux density (mJy)
A	06:58:15.9	−55:56:30.6	0.09 ± 0.02	0.15 ± 0.02	√	70	–	–	–
B	06:58:16.6	−55:58:24.7	0.16 ± 0.02	0.46 ± 0.03	√	110	–	–	–
C	06:58:19.3	−55:58:41.7	0.63 ± 0.02	0.67 ± 0.02	×	90	-0.5 ± 0.1	0.6 ± 0.1	0.6 ± 0.1
D	06:58:20.5	−55:56:20.3	0.08 ± 0.02	0.19 ± 0.02	√	90	–	–	–
E	06:58:23.4	−55:56:41.7	0.78 ± 0.02	0.88 ± 0.02	×	100	-1.00 ± 0.08	0.7 ± 0.1	0.8 ± 0.1
F	06:58:24.0	−55:57:19.6	0.12 ± 0.02	0.13 ± 0.02	×	50	–	–	–
G	06:58:24.0	−55:55:15.2	0.21 ± 0.02	0.35 ± 0.02	√	90	–	–	–
H	06:58:24.6	−55:55:12.2	0.38 ± 0.02	0.46 ± 0.02	×	90	-1.3 ± 0.1	0.4 ± 0.1	0.4 ± 0.1
I	06:58:26.1	−55:55:48.3	0.12 ± 0.02	0.14 ± 0.02	×	90	–	–	–
J	06:58:27.3	−55:56:07.4	0.27 ± 0.02	0.37 ± 0.02	√	80	-0.6 ± 0.2	0.3 ± 0.1	0.3 ± 0.2
K	06:58:34.1	−55:57:53.7	0.50 ± 0.02	0.59 ± 0.02	×	100	-0.8 ± 0.1	0.5 ± 0.2	0.5 ± 0.2
L	06:58:37.9	−55:57:25.4	8.18 ± 0.02	14.66 ± 0.03	√	130	-0.82 ± 0.01	9.4 ± 0.2	13.7 ± 0.2
M	06:58:42.1	−55:58:37.6	7.74 ± 0.02	25.75 ± 0.04	√	100	-0.93 ± 0.01	9.8 ± 0.2	24.0 ± 0.2
N	06:58:44.8	−55:55:25.4	0.47 ± 0.02	0.52 ± 0.02	×	50	0.6 ± 0.1	0.5 ± 0.1	0.5 ± 0.2

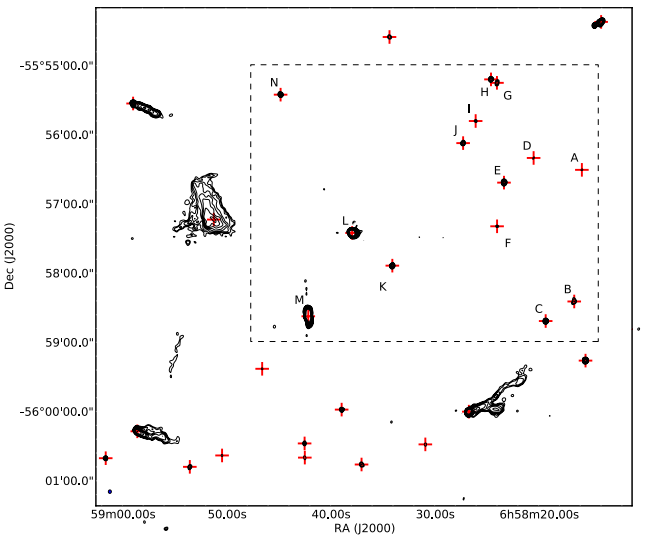

Figure 3. The primary beam corrected Stokes *I* image with the highest resolution (synthesized beam FWHM ≈ 2.7 arcsec) at which we have mapped the data. Data from baselines shorter than 4000λ (corresponding to 50 arcsec) have been excluded to resolve out the extended halo. The dashed rectangle shows the CLEAN box in which we subtract the CLEAN components that were created in this high-resolution imaging process. This image is before the CLEAN components have been subtracted. The contour levels are at $\sqrt{1, 2, 4, 8, \ldots} \times 5 \times 15$ μJy beam^{-1}. The locations of detected sources are shown with crosses, and the properties of sources whose emission contaminates the halo are given in Table 2.

where I_0 and I_1 are images that correspond to the first two coefficients in the Taylor expansion of the sky brightness, ν is the frequency under consideration and ν_0 is the reference frequency which we set to 2.1 GHz. By assuming that sources are described with a spectral index, α, such that

$$I_\nu = I_{\nu_0} \left(\frac{\nu}{\nu_0} \right)^\alpha, \quad (2)$$

a comparison of equation (1) with the Taylor expansion around I_{ν_0} of equation (2) gives $I_{\nu_0} = I_0$ and $\alpha = \frac{I_1}{I_{\nu_0}}$. Images of both I_{ν_0} and α were produced during the multi-frequency multi-scale imaging (see Rau & Cornwell 2011 for a thorough description of this algorithm). This algorithm also produces an $\alpha_{\rm error}$ image, where the errors are dependent upon the bandwidth, number of independent measurements, the *uv*-coverage and the signal-to-noise ratio. To obtain accurate spectra away from the pointing centre, we used the task *widebandpbcor*, which uses a polynomial fit to the ATCA primary beam to make corrections to flux estimates prior to the creation of spectral index images. We note that CASA is capable of using additional Taylor terms to model the spectral curvature; for example, if three Taylor terms are used, the spectrum of a source is described as $I_\nu = I_{\nu_0}(\frac{\nu}{\nu_0})^{\alpha+\beta\log(\nu/\nu_0)}$. However, using additional Taylor terms requires high signal-to-noise. Little spectral curvature is expected for 1E 0657−55.8 in any case, since Liang et al. (2000) showed that, within the error bars, there is no spectral curvature between 0.843 and 8.8 GHz for this radio halo.

3.4.2 *Narrow-band method*

We split the 1.1–3.1 GHz band into successive 290 MHz sub-bands, and imaged each of these sub-bands with the same pixel size and a *uv*-tapering that corresponds to a desired resolution before correcting for the primary beam. This produces a cube containing images at different frequencies but with approximately the same resolution; thus, for each pixel we have flux measurements in each 290 MHz sub-band. Every plane of the cube was convolved with a Gaussian to give all planes exactly the same resolution. To create a spectral index map we found, for each pixel, the power law that best described the flux density of that pixel as a function of frequency. We propagated the errors in our flux estimates to errors in the calculated spectral index, and then blanked out pixels with errors larger than 0.3. Additionally, we blanked pixels where the pixel flux did not exceed five times the noise in all 290 MHz sub-bands.

3.5 Polarization imaging and rotation measure synthesis

We have used two techniques to characterize the polarization properties. In the first method, we use rotation measure (RM) synthesis to search for polarized emission; since maximum sensitivity is desired for this, we use the entire wide-band 1.1–3.1 GHz data set. In the second method, we split the 1.1–3.1 GHz band into successive 100 MHz sub-bands and image each sub-band separately to determine the polarized intensity as a function of frequency for polarized objects. We use the pre-source subtracted data set (see Section 3.3) for both of these polarization analyses.

3.5.1 RM synthesis

The procedure we have used for RM synthesis (Brentjens & de Bruyn 2005) is the same as was used by O'Sullivan et al. (2012). A thorough description is presented in that paper but here we present a summary of the procedure.

After calibration of the 1.1–3.1 GHz data set (see Section 3.1) the Stokes *I*, *Q*, *U* and *V* data were imaged in 10 MHz sub-bands; in this process each sub-band was imaged with approximately the same resolution and CLEANed to five times the thermal noise. The images were then each convolved with a Gaussian to give them exactly the same resolution. The resulting *Q* and *U* image cubes were used to calculate the Faraday dispersion function, which describes the complex polarized surface brightness per unit Faraday depth and is calculated for each pixel (α, δ):

$$F(\phi, \alpha, \delta) \approx \frac{\sum_{i=1}^{N} w_i P_{i,\alpha,\delta} \mathrm{e}^{-2i\phi(\lambda_i^2 - \lambda_0^2)}}{\sum_{i=1}^{N} w_i}, \quad (3)$$

where the sum is over channels, ϕ is the Faraday depth, α is the right ascension, δ is the declination, $w_i P_{i,\alpha,\delta}$ is the weighted complex polarized intensity ($P = Q + iU$) for a pixel and λ_0 is the weighted mean λ^2 over all channels – we find $\lambda_0 = 0.15$ m. The weighting is $w_i = \frac{1}{\sigma^2_{Q,U}}$, where $\sigma_{Q,U}$ is the thermal noise level of the appropriate *Q* and *U* image.

The Faraday dispersion function was calculated for integer values of ϕ between -1750 and 1750 rad m^{-2} to produce an Faraday depth cube, with each slice showing the complex polarization for a different value of ϕ. Fig. 4 shows the amplitude of the rotation measure spread function (RMSF) for our 1.1–3.1 GHz data set, in which bad data have been flagged and 10 MHz sub-bands have been weighted according to their thermal noise levels. For our analysis of the data, the FWHM of the RMSF is 84 rad m^{-2}, the largest detectable scale is 320 rad m^{-2} and the maximum observable Faraday depth is 1650 rad m^{-2}.

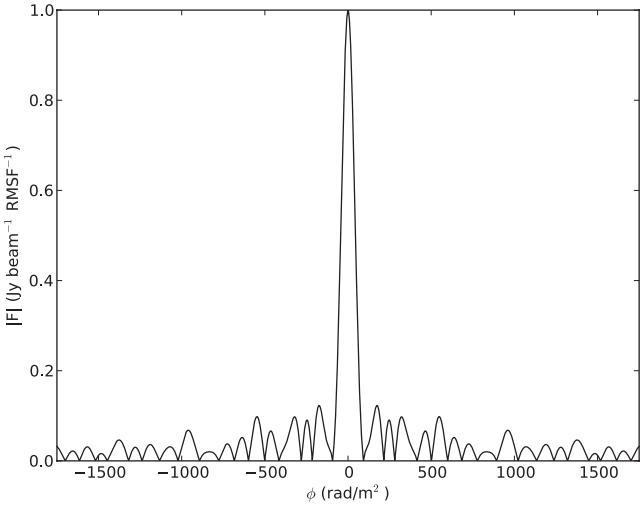

Figure 4. The amplitude of the RMSF for the 1.1–3.1 GHz ATCA polarization data.

As we simply want to detect polarization, we have not attempted to use RMCLEAN (Heald, Braun & Edmonds 2009). Additionally, we do not take into account the spectral index of the Stokes *I* intensity in our calculation of the Faraday dispersion function (see section 3 of Brentjens & de Bruyn 2005).

3.5.2 Polarization as a function of frequency

To study polarization variations of faint sources as a function of frequency, we must compromise between the bandwidth required to make sensitive measurements and the effects of bandwidth depolarization. We split the wide-band 1.1–3.1 GHz data set into multiple 100 MHz sub-bands, and for each of these sub-bands we created images of the Stokes *Q* and *U* data. Polarized intensity images were created from these images ($P = \sqrt{Q^2 + U^2}$). The polarization images were corrected for the Ricean bias and pixels with polarized intensities of less than $2\sigma_{Q,U}$ were flagged. To determine the polarization as a function of frequency for a source, we integrated the pixels within the region of the source that had a polarized flux greater than five times the noise (where we use $\sigma_{Q,U}$ for the noise). This procedure was performed on each of the sub-band polarization images to measure polarization changes as a function of frequency. The errors that we provide on this measurement are $\sigma_{Q,U}$ multiplied by the square root of the source area in synthesized beams.

4 RESULTS

In Fig. 2, we show the 1.1–3.1 GHz image of the bullet cluster, 1E 0657−55.8. Faint large-scale emission is observed just north of the centre of the image; this is the radio halo and is the primary focus of this paper. To the south-east of the radio halo is LEH2001 J06587−5558 (labelled J06587−5558), this source was studied in Liang et al. (2001) but we have used our wide-band observations to provide some new measurements of its properties. The bright source with a large north–south extension that lies on the eastern edge of the radio halo has the spectral and polarimetric properties expected for a radio relic, but we leave a detailed discussion of this source to a forthcoming publication (Shimwell et al., in preparation). Three tailed radio sources are visible to the south, south-east and north-east of the radio halo (see Fig. 2 and the higher resolution image shown in Fig. 3), and a further tailed radio source is located just outside the image at 06:58:43.4 −56:02:35.3 – these tailed radio sources are not discussed further in this publication.

4.1 Radio halo

The radio halo associated with 1E 0657−55.8 was discovered and well characterized by Liang et al. (2000), but our 1.1–3.1 GHz data are deeper. The 1.1–3.1 GHz low-resolution continuum and spectral properties of the halo (post-source subtraction) and surrounding region are presented in Fig. 5; higher resolution images are shown in Fig. 6. In the high-resolution images, the halo flux per synthesized beam is low but the structure of smaller angular scale sources can be examined. As the resolution is decreased, the halo flux per beam increases and the emission from the halo is visible over a large angular scale. We note that the subtraction of contaminating sources,

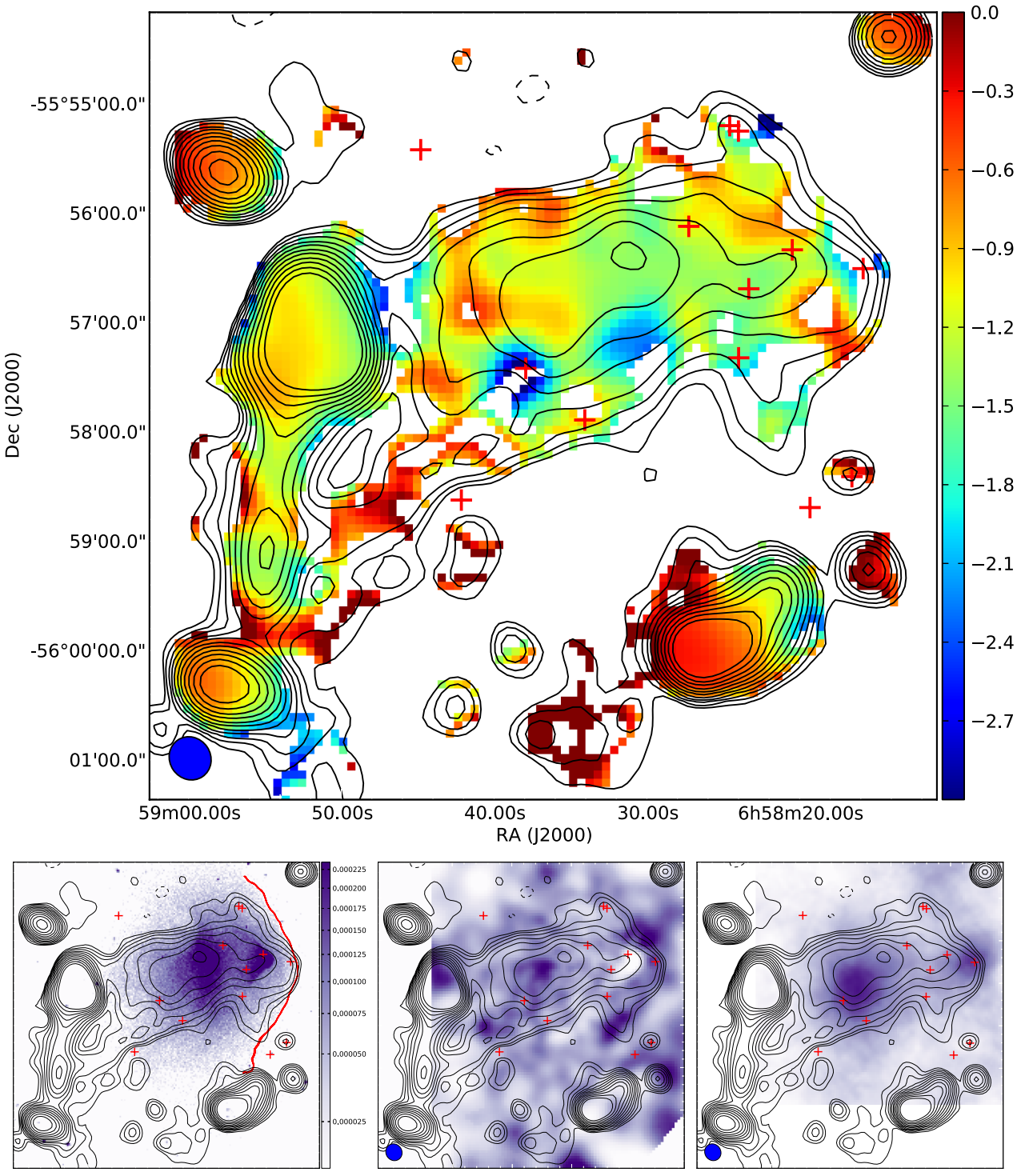

Figure 5. Top: the contours show the 1.1–3.1 GHz primary beam corrected continuum emission of the radio halo at a resolution of 23.3 arcsec. The colour scale shows the 1.1–3.1 GHz spectral index image at the same resolution which was created using the wide-band method described in Section 3.4.1. All regions on the spectral index image where the error exceeds 0.3 have been blanked, and the errors on this 1.1–3.1 GHz spectral index image are presented in Fig. 9. Images at different resolutions are shown in Fig. 6. Bottom left: low-resolution ATCA contours overlaid on a colour scale image made from 500 ks of *Chandra* ACIS-I data from the 0.8–4 keV band (see Markevitch 2006). The scale is in counts s^{-1} $pixel^{-1}$ (the pixel size is 1.968 arcsec) and the red line shows the X-ray shock front (as defined by Chung et al. 2009, i.e. tracing out constant X-ray intensity from 06:58:24.0 −55:54:06.0 to 06:58:24.0 −55:44:28.8). Bottom centre: low-resolution ATCA data overlaid on an X-ray temperature image with the scale in keV (Markevitch, in preparation; see also Owers et al. 2009). Bottom right: low-resolution ATCA contours overlaid on a colour scale corresponding to the weak-lensing reconstruction presented by Clowe et al. (2006). The colour scale is in weak-lensing κ units and can be converted to solar masses per pixel (the pixel size is 3.552 arcsec) with a conversion factor of 7×10^{11} $M_{\odot}$ $pixel^{-1}$. The weak-lensing data are from http://flamingos.astro.ufl.edu/1e0657/public.html. For all images, the ellipse in the bottom-left corner shows the ATCA synthesized beam and the contour levels are $5 \times \sqrt{1, 2, 4, 8, \ldots} \times 25$ μJy $beam^{-1}$; positive contours are solid lines and negative contours are dashed. All images have been primary beam corrected.

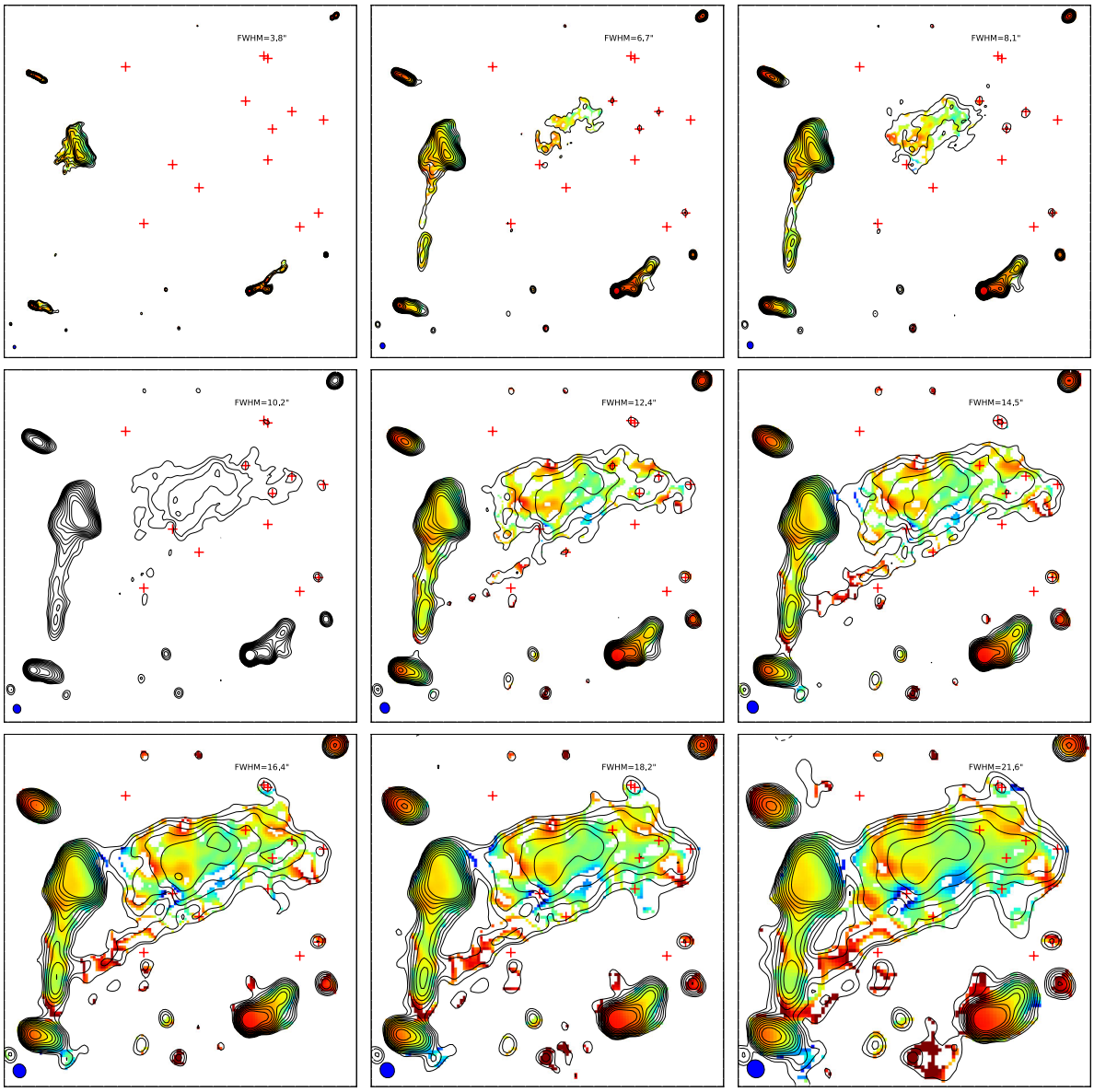

Figure 6. The same as the top panel of Fig. 5 but for images created at resolutions ranging from 3.8 to 21.6 arcsec. The synthesized beam is shown in the bottom-left corner of the images and its FWHM is displayed on the image. The axis labels, colour scale and contour levels are identical to those in Fig. 5. The spectral index images are blanked for regions where the error exceeds 0.3.

particularly source M, is not perfect and artefacts remain on the image. In all source subtracted images that we present, we show the locations of the subtracted sources so that these regions can be interpreted with caution.

In comparison to the Liang et al. (2000) continuum images of the halo (fig. 5 of that paper), our detection is at higher significance and the morphology of the halo is more precisely characterized, with sharp edges to the radio halo emission rather than low signal-to-noise poorly defined edges that hinder accurate characterization and comparison to other data sets. Nevertheless, the Liang et al. (2000) observations did reveal that the halo was extended along the merging axis, in agreement with our observations of an ≈130 arcsec extension in the north–south direction compared to the ≈270 arcsec extension in the east–west direction. A key morphological difference is the distinctive radio halo edge on the western side of the halo that we see in Fig. 5 which was not apparent in previous data.

We measure the integrated radio halo flux and its variation with frequency on low-resolution narrow-band (see Section 3.4.2) pre-source subtracted images. We have conducted the measurements over two regions: (a) the 100 μJy beam^{-1} contour level shown in Fig. 5 that is within the right ascension range 06:58:15 to 06:58:46 and declination range −55:55:00 to −55:58:45 but not within 30 arcsec of source M (area 8.5 arcmin^2); (b) the CLEAN box shown in Fig. 3 (area 18.4 arcmin^2). We subtracted the flux of sources within the regions of integration using the parameters in Table 2 (for sources where we were unable to measure the spectral properties we use the 1.1–3.1 GHz flux to approximate the 2.1 GHz flux and assume $\alpha_{1.1}^{3.1} = -0.7 \pm 0.5$) and propagate the errors into our measurements of the integrated radio halo flux. From the smaller area, we find an integrated 2.1 GHz flux of 24.7 ± 1.5 mJy and $\alpha_{1.1}^{3.1} = -1.57 \pm 0.05$, and from the larger area we find an integrated 2.1 GHz flux of 27.5 ± 1.7 mJy and $\alpha_{1.1}^{3.1} = -1.50 \pm 0.04$.

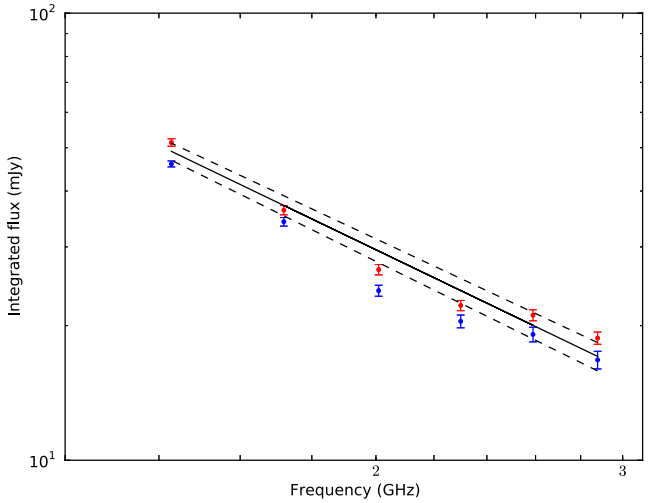

Figure 7. The frequency dependence of the integrated flux of the radio halo after contaminating sources has been removed. The blue points were measured from the region within the 100 μJy beam^{-1} contour level shown in Fig. 5 that is within the right ascension range 06:58:15 to 06:58:46 and declination range −55:55:00 to −55:58:45 but not within 30 arcsec of source M. The red points were measured from within the CLEAN box region shown in Fig. 3. The solid line shows the best fit to the integrated flux measurement from the larger area and the dashed lines show the errors on this fit.

Our measurements of the integrated halo properties are presented in Fig. 7.

We have measured the spectral index across the halo in two ways (see Section 3.4); spectral index images created at low resolution using the wide-band and narrow-band methods are shown in Figs 5 and 8, respectively (the wide-band spectral index error image is shown in Fig. 9). The two spectral index methods produce consistent results and are in agreement with our derived spectral index of the integrated halo flux. The spectral index images reveal that the central

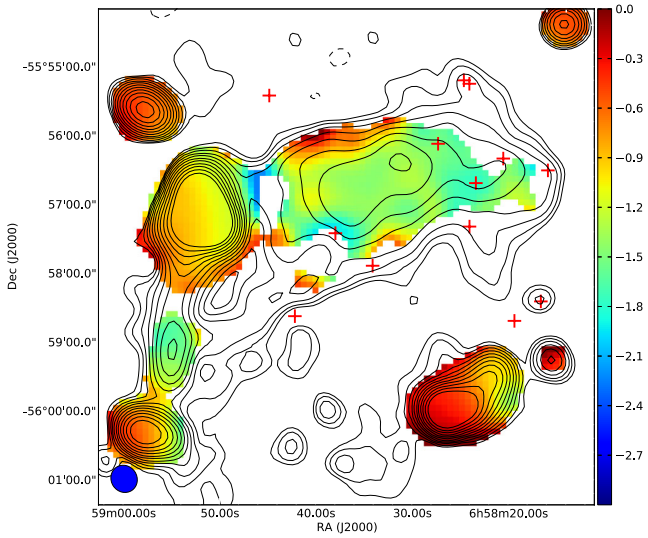

Figure 8. A low-resolution (synthesized beam FWHM equals 28.6 arcsec) spectral index map created from the narrow-band method described in Section 3.4.2. All pixels with errors greater than 0.3 are blanked. In regions where we were able to determine the spectral index, this spectral index map is consistent with the spectral index map created using the wide-band method (see Section 3.4.1) which is shown in Fig. 5. The contour levels are identical to those in Fig. 5.

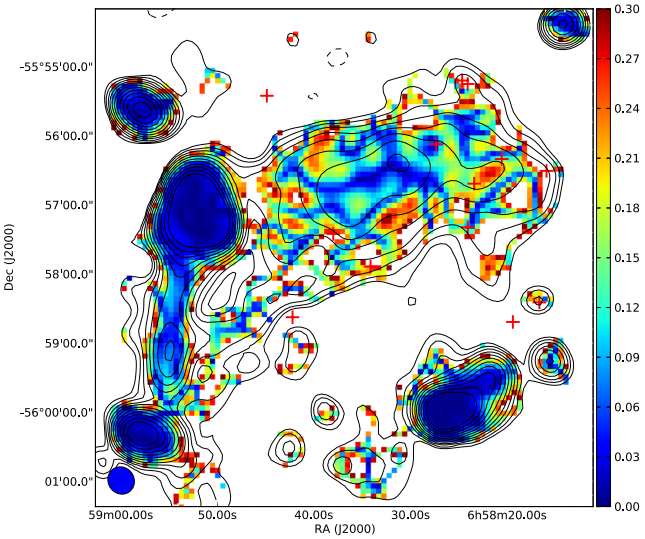

Figure 9. The spectral index error image for the 1.1–3.1 GHz spectral index map in Fig. 5 that was created using the wide-band method described in Section 3.4.1. The maximum spectral index error is 0.3. The contour levels are identical to those in Fig. 5.

region of the halo has a spectral index of $\alpha_{1.1}^{3.1} \approx -1.4$ and that there are variations in the spectral index across the halo.

We have used RM synthesis to search the wide-band data set for polarized emission. We created RM cubes from the 1.1–3.1 GHz data set (see Section 3.5.1) at resolutions of 17 and 21 arcsec; Fig. 10 shows several planes of the low-resolution RM cube. In the region of the halo, the standard deviation of the Stokes Q and U components, $\sigma_{Q,U}$, of the complex RM cube varied with RM significantly (see Fig. 11), with lower noise levels obtained at large positive or negative RM away from all the signal in the Q and U images. We searched through the RM cubes in the region of the radio halo (which we defined as right ascension 06:58:15 to 06:58:45 and declination −55:55:00 to −55:58:00) for polarized emission that exceeded $5\times\sigma_{Q,U}$, but were unable to detect any emission. The peak intensity of the 1.1–3.1 GHz Stokes I images is 1.3 mJy beam^{-1} at 21 arcsec and 0.8 mJy beam^{-1} at 17 arcsec, while the maximum $5\sigma_{Q,U}$ of the $F(\phi)$ spectrum at these resolutions is 170 and 130 μJy beam^{-1} RMSF^{-1}, respectively. The non-detection of polarized emission implies that in the region of peak radio emission, the fractional polarization in the 1.1–3.1 GHz images is less than 13 per cent when observed with 21 arcsec resolution and less than 16 per cent at 17 arcsec resolution.

To calculate a limit on fractional polarization at 1.4 GHz, we used the narrow-band polarization technique described in Section 3.5.2. For a 20 arcsec resolution polarization image of a 100 MHz wide band centred at 1.48 GHz, in which $\sigma_{Q,U}$ is 54 μJy beam^{-1} RMSF^{-1}, we found no polarized emission at greater than $5\sigma_{Q,U}$ within the region of the radio halo. From our narrow-band images, we estimate a radio halo peak flux of 3.1 mJy beam^{-1} at 1.48 GHz, and therefore our $5\sigma_{Q,U}$ upper limit on the fractional polarized intensity at this frequency is 9 per cent.

4.2 LEH2001 J06587−5558

J06587−5558 is a steep spectrum, extremely polarized, extended, extragalactic source observed coincident with the south-east peripheral region of 1E 0657−55.8 (source M in Fig. 3 and Table 2). A study of this source was presented by Liang et al. (2001), who

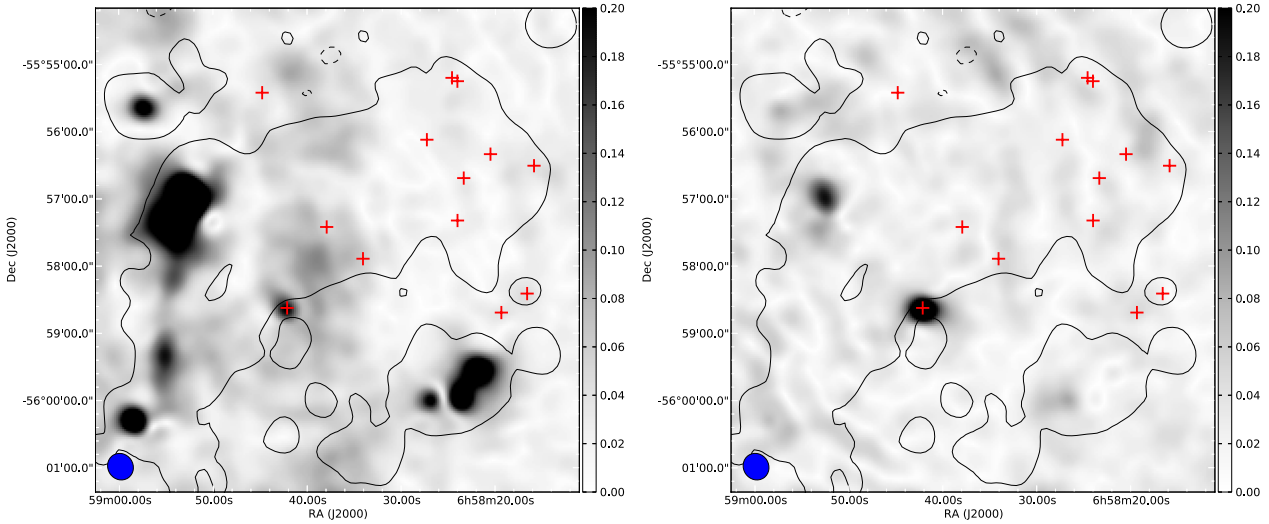

Figure 10. Left: polarized intensity image at RM $= -30$ rad m^{-2} where $\sigma_{Q,U} = 31$ μJy beam^{-1}. Right: polarized intensity image at RM $= -236$ rad m^{-2} where $\sigma_{Q,U} = 23$ μJy beam^{-1}. The polarized intensity images are at low resolution (FWHM $= 21$ arcsec) and the grey-scale is in mJy beam^{-1} RMSF^{-1}. The contour shows the 5×25 μJy beam^{-1} level of the source subtracted Stokes *I* image at 23.3 arcsec resolution.

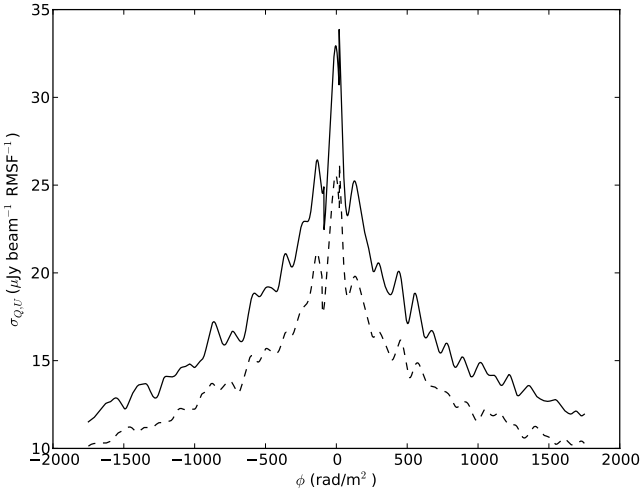

Figure 11. The noise ($\sigma_{Q,U}$) in $F(\phi)$ as a function of ϕ. The dashed line shows the noise when the Q and U images were made with a resolution of 17 arcsec and the solid line shows the noise on the 21 arcsec resolution images. The noise is highest at a wide range of ϕ around $\phi = 0$. In this region, there is more emission from polarized sources in the field.

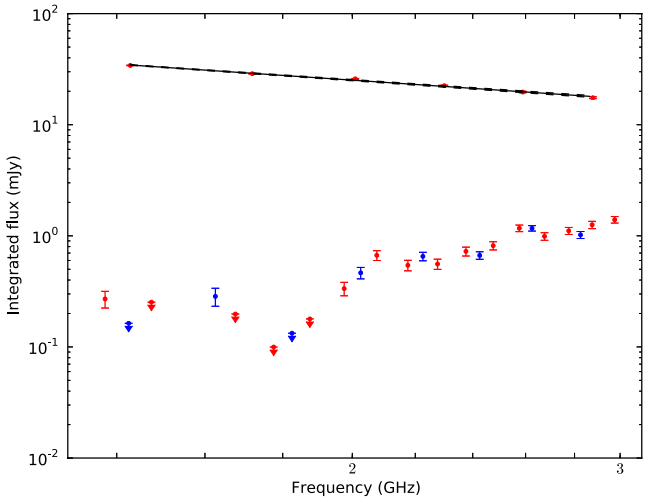

Figure 12. The total intensity and polarization spectral energy distributions over 1.1–3.1 GHz for the source J06587−5558. The red points that have been fitted with a power law (black line) show the Stokes *I* emission from J06587−5558. The unfitted red points show the polarized emission from J06587−5558 where the Stokes Q and U data were imaged in 100 MHz sections. The unfitted blue points again show the polarized emission from J06587−5558 but where the Stokes Q and U were imaged in 200 MHz sections. Upper limits ($5\sigma_{Q,U}$) on the polarized intensity are shown with arrows.

concluded that it is either a gravitationally lensed source, a high-redshift radio galaxy or a cluster relic. They measured a flux density of 37 ± 2 mJy at 1.3 GHz, spectral indices $\alpha_{2.2}^{1.3} = -1.0$ and $\alpha_{8.8}^{4.8} = -1.5$, and found that the source rapidly depolarizes with increasing wavelength, with integrated fractional polarizations of 54 ± 11, 45 ± 9, 4.3 ± 0.5 and <0.5 per cent at 8.8, 4.8, 2.2 and 1.3 GHz, respectively.

From high-resolution Stokes *I* images of J06587−5558, we measure a 1.4 GHz flux of 35.1 ± 0.5 mJy and $\alpha_{3.1}^{1.1} = -0.93 \pm 0.01$, both in agreement with the results of Liang et al. (2001). We find no evidence for a change in spectral index over the observed frequency range (see Fig. 12), and combining this result with the measurements of Liang et al. (2001) indicates that a break in the spectral index must occur between 3.0 and 4.8 GHz. For the polarization analysis, we split the 1.1–3.1 GHz band into 100 MHz sub-bands and follow the procedure outlined in Section 3.5.2 to determine the frequency dependence of the polarized emission from this source. We perform the same analysis but with 200 MHz sub-bands and find that the polarized emission in these wider sub-bands is consistent with measurements from the 100 MHz analysis, indicating that for this analysis we are not significantly affected by bandwidth depolarization. The measured polarization and Stokes *I* flux for this source are given in Fig. 12. In agreement with Liang et al. (2001), we find that the source depolarizes at lower frequency. Our measurements of polarized emission at frequencies less than 2.0 GHz are at low significance but we find that at 1.38 GHz the fractional polarization is 0.8 ± 0.1 per cent. At 2.2 GHz, we measure a fractional polarization of 2.7 ± 0.3 per cent, and this rises to 7.0 ± 0.1 per cent at

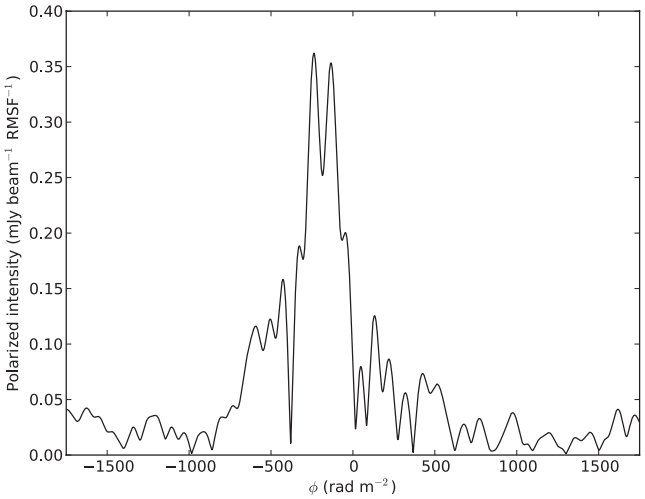

Figure 13. The $F(\phi)$ spectrum at 6:58:42.1 −55:58:37.6, the location of the Stokes *I* peak of J06587−5558.

2.9 GHz. Our 2.2 GHz measurement of the fractional polarization is a little lower than was determined by Liang et al. (2001), and further measurements would be useful to reconcile the difference.

The Galactic magnetic field in the direction of the cluster is $+4.8 \pm 44.0$ rad m^{-2} (Oppermann et al. 2012) but the $F(\phi)$ spectrum of this source reveals that the polarized intensity peaks at $\phi = -238$ rad m^{-2}. This is in agreement with the Liang et al. (2001) measured value of -266 ± 37 rad m^{-2} but, as shown in Fig. 13, the $F(\phi)$ spectrum of this source likely has multiple components.

5 DISCUSSION

In Fig. 5, we compare our low-resolution radio halo image to the observed X-ray brightness (Markevitch 2006) and to the weak-lensing mass reconstruction (Clowe et al. 2006). These images reveal that the morphology of the radio halo and thus the population of synchrotron emitting electrons has similarities to, but does not strictly follow, the X-ray observed bremsstrahlung emission that traces the ICM (see also Fig. 14), nor does it trace the distribution of galaxies that extends well beyond the western edge of the radio halo.

Unlike for the Coma cluster (Giovannini et al. 1993), we do not observe a radial steepening of the spectral index and instead observe that there are localized regions within the spectral index image that are different from the average (see Figs 5, 6 and 8). For example, on the eastern edge of the radio halo (06:58:40 −55:57:00) close to the proposed radio relic, the spectral index is flatter than average; this flattening may be associated with the shock that created the proposed relic or a counter shock of the prominent western bow shock. Alternatively, the lack of an ordered spectral index distribution may be because the halo is young and in formation, with turbulence associated with the ongoing merger still altering its structure.

5.1 Integrated halo properties

Liang et al. (2000) measured an integrated radio halo flux of 78 ± 5 mJy at 1.3 GHz from a large region (32.7 arcmin^2) around 1E 0657−55.8. They also measured an integrated 1.3 GHz flux of ≈50 mJy from the 7.3 arcmin^2 region of bright radio halo emission (see fig. 7 of Liang et al. 2000). Similarly, we have made two measurements of the integrated flux: one over a small area (8.5 arcmin^2), which is entirely filled with significant radio halo emission; and another over a large area (18.4 arcmin^2), which encompasses the halo and surrounding region. From the fit to our measurements of the integrated radio halo flux as a function of frequency, we determine 2.1 GHz (1.3 GHz) integrated flux densities of 24.7 ± 1.5 mJy (52.5 ± 2.1 mJy) and 27.5 ± 1.7 mJy (56.4 ± 2.3 mJy) from the smaller and larger regions, respectively (see Fig. 7). Our measurements are in good agreement with the small-area measurements by Liang et al. (2000). However, a discrepancy arises when the area integrated over is much larger than the region of significant radio emission. Our measurement remains approximately constant with integration area whereas the Liang et al. (2000) measured value rises to 78 ± 5 mJy at 1.3 GHz. Our spectral index measurements ($\alpha_{1.1}^{3.1} = -1.57 \pm 0.05$ and -1.50 ± 0.04) are steeper than the Liang et al. (2000) measurement of $\alpha_{0.8}^{8.8} = -1.3 \pm 0.1$.

Future observations will be necessary to reconcile the difference between our large-area integrated flux estimates and those by Liang et al. (2000) but we note that our flux and spectral index measurements of less complex objects, such as LEH2001 J06587−5558, are in good agreement with the Liang et al. (2000) measurements.

5.2 Radio versus X-ray brightness

Along the east–west axis, we have taken three one-dimensional slices through the X-ray and radio emission (see the left-hand side of Fig. 14), and these show that along this axis the extent and brightness profile of the X-ray emission are similar to those seen in the radio. However, in the north–south direction the extent of the radio halo (≈130 arcsec) is significantly less than that of the X-ray emission (see the top and bottom panels on the right-hand side of Fig. 14). In this cluster system, the smaller cluster (the bullet) has passed through a larger cluster 0.1–0.2 Gyr ago (Markevitch 2006); if merger turbulence were not yet widespread throughout the ICM, this could explain the lack of radio emission in the northern and southern extremities of the cluster. In the direction of the merger, where we would expect significant turbulence, we observe that the halo appears to trace out the path taken by the bullet and extends to the eastern and western extremities of the cluster. The morphology of the halo therefore appears to be consistent with what would be expected from a radio halo still in formation and formed as a consequence of a recent merging event. Furthermore, the observed extension is reproduced in a recent suite of simulations by Donnert (2013), who simulated a radio halo in a system similar to the bullet cluster and found that turbulence behind the infalling cluster accelerates a population of seed non-thermal electrons to produce a stream of relativistic synchrotron emitting electrons.

We find that the peak of the radio halo emission (06:58:31.6 −55:56:29.5) is coincident with the X-ray centroid of the main cluster (see the centre-left panel of Fig. 14) but 35 arcsec (150 kpc) north-west of the weak-lensing centroid [where we have used the X-ray and weak-lensing centroids given by Clowe et al. (2006) as 06:58:30.2 −55:56:35.9 and 06:58:35.3 −55:56:56.3]. However, the bright X-ray structure of the main cluster component is primarily extended in the north–south direction, but the bright region of the radio halo extends primarily to the south-west towards the hottest region in the cluster (excluding the temperatures derived at the shock) and the weak-lensing mass reconstruction centroid. Fig. 14 demonstrates that this misalignment between the X-ray and radio halo emission is predominantly in the direction of the cluster merger; in the direction perpendicular to this the X-ray and radio brightness emission is better aligned. Simulations presented by Donnert (2013), where the origin of radio halo emission is turbulent

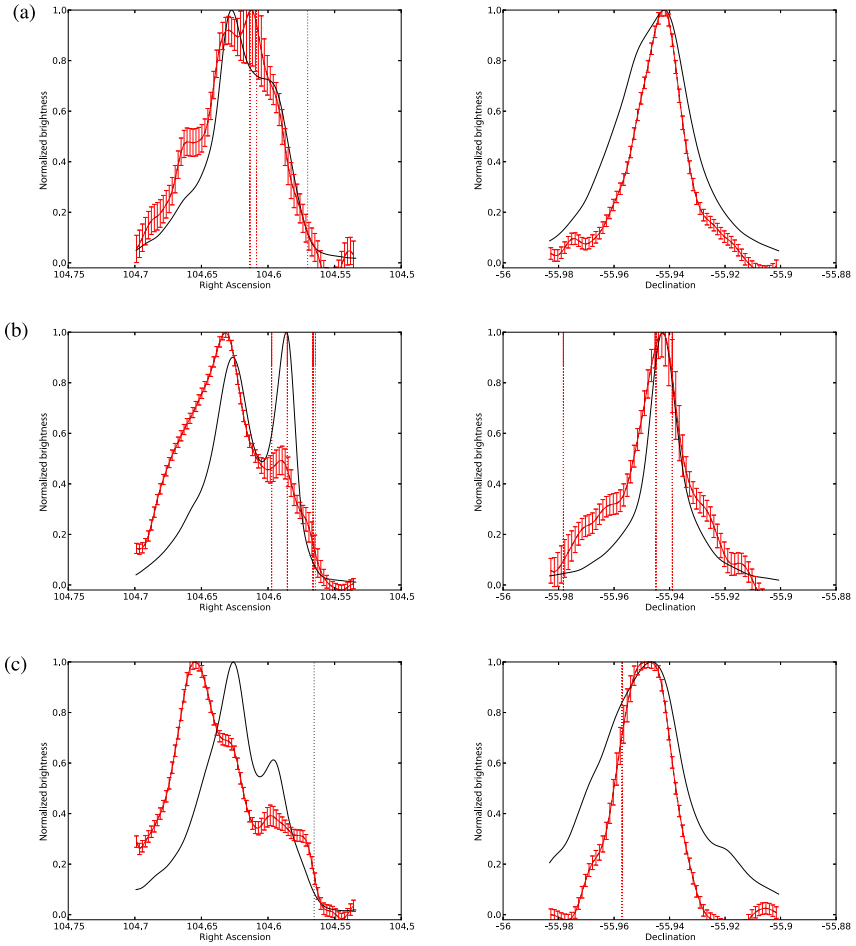

Figure 14. One-dimensional brightness profiles of the X-ray and radio emission. The X-ray emission is shown by solid black lines, the radio emission is shown with solid red lines and the error bars are $\pm(30 + R\exp\frac{-X^2}{2\sigma^2})$ μJy beam^{-1}, where R is the residual flux density after source subtraction (see Table 2), X is the separation of the source from the position in the slice and σ is the synthesized beam standard deviation (FWHM = 23.3 arcsec). The errors shown are thus not simple random errors but also show the maximum contamination from the residuals that remain after CLEAN component subtraction which are not random but will increase the flux. The locations of sources that contribute more than 30 μJy beam^{-1} in errors are shown with red dotted vertical lines. For the slices at constant declination, the location of the X-ray detected shock front is shown by a grey vertical dotted line. The X-ray emission has been convolved with a 20 arcsec Gaussian to aid comparison with the low-resolution radio image. Both the X-ray and radio brightness profiles have been divided by a normalization factor so that they peak at 1.0. On the left from top to bottom, the radio normalization factors are 0.6, 1.5 and 1.3 mJy beam^{-1} and the corresponding X-ray normalization factors are 1.7, 3.0, 2.4 × 10^{-4} counts s^{-1} pixel^{-1}. On the right from top to bottom, the radio normalization factors are 1.3, 0.7, 1.3 mJy beam^{-1} and the corresponding X-ray normalization factors are 2.8, 3.0 and 1.2 × 10^{-4} counts s^{-1} pixel^{-1}. (a) Left: a slice through right ascension at a declination of −55:56:00.0. Right: a slice through declination at right ascension 06:58:30.0. The slice through declination also passes close (3 arcsec) to the peak in the centroid of the X-ray emission from the main cluster at 55.°94. (b) Left: a slice through right ascension at a declination of −55:56:30. Right: a slice through declination at a right ascension of 06:58:21.2. These slices pass through the X-ray centroid of the smaller cluster (the bullet). In the slice through right ascension, an increase in the radio halo brightness is visible close to the position of the bullet (the bullet is clearly seen in the X-ray profile at a declination of 104.°58). The slice through right ascension also passes close (6 arcsec) to the peak in the centroid of the X-ray emission from the main cluster at 104.°62 and through the peak the radio halo emission at 104.°63. (c) Left: a slice through right ascension at a declination of −55:57:00. Right: a slice through declination at a right ascension of 06:58:36.

acceleration, also show a misalignment between the radio and X-ray emission in the direction of the cluster merger.

Constraining our search of a radio halo peak to the region surrounding the bullet, we find a radio halo peak at 06:58:23.6 −55:56:43.0 which is offset by 20 arcsec (88 kpc) eastwards from the centroid of the X-ray emission from the bullet (06:58:21.2 −55:56:30.0) and 65 arcsec (270 kpc) eastwards from the centroid of the weak-lensing mass reconstruction of the bullet (06:58:16.0 −55:56:35.1). The small radio brightness peak can also be seen in the centre-left panel of Fig. 14; although there are two subtracted sources whose residuals introduce additional uncertainty, the faint peak appears real but is a low-significance detection. We note that the errors shown in Fig. 14 are not simply random errors; instead they consist of 30 μJy beam^{-1} random errors plus a maximum contamination from the residuals that remain after CLEAN component subtraction (in this region these are around 50 μJy beam^{-1}), which will increase the flux in this region. The presence of a second peak in the radio halo brightness suggests that the halo could have two components, one associated with the main cluster and another associated with the bullet.

On the western tip of the radio halo, the north–south extent is small but initially it increases smoothly as a function of distance from the western tip. The north–south extent reaches a maximum of ≈230 arcsec about ≈1 arcmin from the western tip after which

it rapidly decreases to about ≈130 arcsec and maintains this north–south extent across the rest of the halo. This maximum in the north–south extension of the halo is approximately equal in extent to the X-ray emission, and in this region the brightness profiles of the X-ray and radio emission are similar (see Fig. 5 and the centre-right panel of Fig. 14). In contrast, as previously mentioned, the rest of the cluster has an X-ray morphology that extends beyond the radio halo emission in the north–south direction. These northern and southern extensions of the radio halo are faint, and are only visible close to the shock that precedes the bullet as it propagates through the larger cluster. A possibility is that the shock is partially responsible for the emission and indeed, the distinctive shape of the western edge of the halo mimics that of the X-ray detected shock front with Mach number $M = 3.0 \pm 0.4$ (Markevitch 2006). To demonstrate this morphological similarity, in Fig. 5 we have overlaid the X-ray shock on the radio halo emission and see excellent correspondence. The efficiency with which shocks at this low Mach number can accelerate electrons or protons (which could then decay to produce the relativistic electrons) is unknown (e.g. Kang & Jones 2007; Riquelme & Spitkovsky 2011; Kang, Ryu & Jones 2012). However, our observations of the radio halo of 1E 0657−55.8 indicate that merger shocks play a major role in the formation of radio haloes and show that even this low Mach number shock can instigate synchrotron emission.

5.3 Correlations

It has been observed that there is a trend for clusters with high X-ray temperatures to have flatter radio halo spectra (see Feretti et al. 2004; Giovannini et al. 2009; Venturi et al. 2013). Furthermore, several studies (e.g. Feretti et al. 2001; Govoni et al. 2001; Giacintucci et al. 2005) have found that for regions within a single cluster, there is a positive correlation between radio halo luminosity and X-ray luminosity. We have performed a point-to-point comparison of our radio brightness and spectral index images with the X-ray and weak-lensing mass reconstruction images, using the grid shown in Fig. 15. Using the same procedure as Govoni et al. (2001), we estimate the errors from the standard deviation of pixels within the grid cells. Fig. 16 shows the observed correspondence between the X-ray, weak-lensing and radio properties. For each of these plots, we calculate the Spearman's rank correlation coefficient (ρ); the non-parametric nature of this correlation coefficient allows us to identify whether there is a monotonic relationship between variables. From the correlation coefficient, we determine the z-score (z_s), which can be interpreted as the Gaussian significance of correlation:

$$z_s = F(\rho)\sqrt{\frac{N-3}{1.06}}, \quad (4)$$

where $F(\rho)$ is the Fisher transformation of the Spearman rank correlation coefficient and N is the number of data pairs. To propagate the uncertainty from our measurement values, we use a Monte Carlo analysis where we resample each measurement from a Gaussian distribution centred on the mean with a standard deviation equal to the measurement error. These resampled values form a new measurement set for which we calculate ρ and z_s. Repeating the procedure a statistically robust number of times produces a Gaussian distribution of z-scores from which we calculate the mean, which is our significance of correlation, and the standard deviation, which is our error on this significance of correlation. The results are given in Table 3, and demonstrate that we detect no significant correlations between the radio and weak-lensing or radio and X-ray parameters.

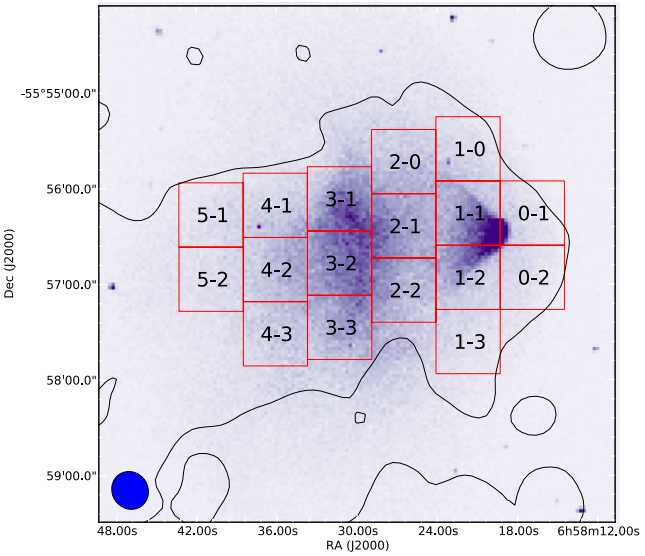

Figure 15. The labelled 40 arcsec × 40 arcsec red boxes show the regions used for a point-to-point comparison between images. The X-ray emission is shown in colour, and the solid line shows the 25 μJy beam^{-1} contour level of the low-resolution radio image (synthesized beam FWHM equals 23.3 arcsec).

Given that some of these correlations have been observed in some clusters, in particular the relation between X-ray and radio halo brightness which can be a tight correlation (see e.g. Govoni et al. 2001), the lack of a detected correlation indicates that this radio halo may be in a different state from those obeying the scaling relation which typically have a more circular appearance. The absence of the scaling relation could be due to a number of things, such as the extreme merging state of this cluster leading to a complex distribution of thermal and non-thermal gas; the large variations in temperature across the cluster; projection effects; or that the radio halo may still be forming and is in a different stage of its evolution than those that obey the scaling relations. Alternatively, there could be two components to this halo, each obeying a scaling relation, and the observed signal showing the combined emission not strictly following the relations. However, this second hypothesis seems unlikely, because if we remove the data from the three western grid columns in Fig. 15 from the Spearman rank calculations, thus leaving just the regions close to the main cluster, we find no improvement in the significance of correlation.

5.4 Polarization

To date, polarization has been very difficult to detect in radio haloes, with the only detected polarized emission being filamentary structures in the clusters A2255 and MACS J0717+3745 (Govoni et al. 2005; Bonafede et al. 2009; Pizzo et al. 2011). Cluster-wide polarized emission that is indisputably associated with a radio halo has not been detected in any cluster. Beam depolarization is thought to be a major cause for these non-detections. This agrees with recent simulations by Govoni et al. (2013, fig. 4), who show that the fractional polarization at the centre of a simulated cluster is 2, 3 and 7 per cent when observed with resolutions of 50, 30 and 10 arcsec, respectively. The simulations predict that the centre of the cluster has the lowest fractional polarization (due to internal depolarization), but as it is the brightest region of the halo in Stokes I, it is still the region of highest polarized surface brightness. In the case of the

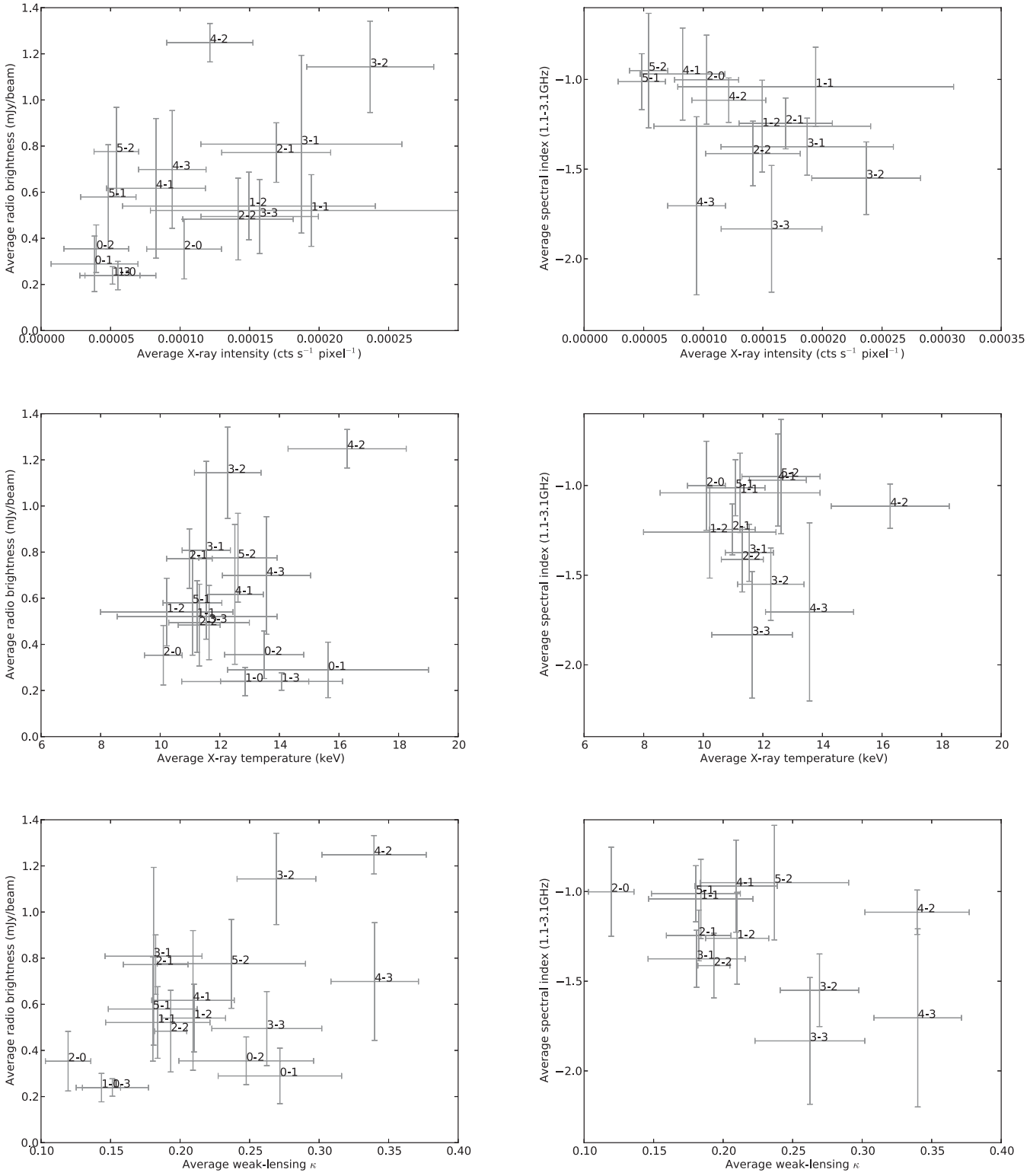

Figure 16. Point-to-point comparison of the radio image and wide-band spectral index map with the X-ray and weak-lensing images. Each point is labelled corresponding to its position in the grid shown in Fig. 15.

bullet cluster, we may also expect the shock on the western edge to align the magnetic field and for the observable fractional polarization in this region to be higher than usual (radio relics, which are thought to be caused by shocks, are often 20–30 per cent polarized). However, we have not been able to detect any polarized emission from within the region of the radio halo. Our $5\sigma_{Q,U}$ limits on the fractional polarization of 13 per cent when observed with 21 arcsec resolution and 16 per cent at 17 arcsec resolution are still significantly higher than Govoni et al. (2013) predictions of the radio halo polarized emission. These limits are from wide-band 1.1–3.1 GHz

Table 3. Derived z-scores and Spearman rank correlation coefficients together with their corresponding errors for the plots presented in Fig. 16. In parentheses, we present the same parameters but derived from the narrow-band spectral index image (Fig. 8) rather than the wide-band spectral index image (Fig. 5). No significant correlation is observed between the radio and weak-lensing or radio and X-ray parameters.

x-axis	y-axis	z_s	ρ
X-ray intensity	Radio brightness	1.6 ± 0.7	0.4 ± 0.2
X-ray intensity	Spectral index	-1.2 ± 0.8	-0.4 ± 0.2
		(-0.8 ± 0.8)	(-0.3 ± 0.2)
X-ray temperature	Radio brightness	0.0 ± 0.7	0.0 ± 0.2
X-ray temperature	Spectral index	-0.1 ± 0.8	0.0 ± 0.3
		(0.1 ± 0.7)	(0.0 ± 0.3)
Weak lensing	Radio brightness	1.5 ± 0.7	0.3 ± 0.2
Weak lensing	Spectral index	-1.0 ± 0.8	-0.3 ± 0.2
		(-0.3 ± 0.8)	(-0.1 ± 0.3)

images, whereas the Liang et al. (2000) limits (3σ limits at 20, 6.5 and 1.4 per cent at resolutions of 10, 20 and 60 arcsec, respectively) are at 1.4 GHz. Our 1.4 GHz limits are comparable to those of Liang et al. (2000).

6 CONCLUSIONS

We have analysed deep, wide-band, polarimetric, radio observations of the bullet cluster. After removing the contamination from radio sources, we have presented images of the bullet cluster radio halo that have significantly better sensitivity than previously published images of this halo. From these observations, we have been able to characterize the morphology and spectral properties of the radio halo, but have been unable to detect polarized emission from any regions of the halo. From our study, we have found the following.

(i) We determined an integrated 1.3 GHz flux density of 52.5 ± 2.1 mJy from the region of significant radio halo emission. In this region, our measurements are in good agreement with the Liang et al. (2000) measurements from a comparable region. However, when integrating over a region much larger than the area of significant emission, we measure an integrated 1.3 GHz flux density of 56.4 ± 2.3 mJy which is lower than the large-area Liang et al. (2000) measurement of 78 ± 5 mJy.

(ii) Our measured 1.3 GHz to 3.1 GHz spectral index (-1.57 ± 0.05) is steeper than the 0.8 GHz to 8.8 GHz spectral index measured by Liang et al. (2000) (-1.3 ± 0.1).

(iii) The radio emission extends as far as the observed X-ray emission in the direction of the cluster merger, but perpendicular to this axis; the extent of the radio emission is smaller than that of the X-ray emission.

(iv) We find evidence for two peaks in the radio halo emission. One is coincident with the X-ray centroid of the main cluster and another is close to the bullet.

(v) The centroids of surface brightness slices through the halo and X-ray structures are better aligned in the direction perpendicular to the merging axis than in the direction of the cluster merger.

(vi) There is a distinctive edge to the bullet cluster radio halo, which is coincident with the bow shock detected in deep X-ray observations.

(vii) The radio intensity and spectral index distribution do not have tight correspondences with the X-ray brightness, X-ray temperature or weak-lensing mass reconstruction.

(viii) The radio spectral index varies across the cluster but there is no clear trend.

(ix) We do not detect any polarized emission from the radio halo. Our $5\sigma_{Q,U}$ upper limits on the fractional polarization in the centre of the cluster over the 1.1–3.1 GHz band are 13 per cent at a resolution of 21 arcsec.

ACKNOWLEDGEMENTS

We thank the anonymous referee for their comments. The Australia Telescope Compact Array is part of the Australia Telescope National Facility which is funded by the Commonwealth of Australia for operation as a National Facility managed by CSIRO. We also thank Maxim Markevitch for useful discussions and for kindly providing X-ray brightness and temperature images. We thank Amy Kimball for comments which improved this paper. BMG acknowledges the support of Australian Laureate Fellowship FL100100114 from the Australian Research Council.

REFERENCES

Akamatsu H., Kawahara H., 2013, PASJ, 65, 16
AMI Consortium: Franzen T. M. O. et al., 2011, MNRAS, 415, 2699
AMI Consortium: Shimwell T. W. et al., 2013, MNRAS, 433, 2920
Bonafede A. et al., 2009, A&A, 503, 707
Bourdin H., Mazzotta P., Markevitch M., Giacintucci S., Brunetti G., 2013, ApJ, 764, 82
Brentjens M. A., de Bruyn A. G., 2005, A&A, 441, 1217
Briggs D. S., 1995, PhD thesis, New Mexico Institute of Mining Technology
Brown S., Rudnick L., 2011, MNRAS, 412, 2
Brüggen M., Bykov A., Ryu D., Röttgering H., 2012, Space Sci. Rev., 166, 187
Brunetti G., Setti G., Feretti L., Giovannini G., 2001, MNRAS, 320, 365
Chung S. M., Gonzalez A. H., Clowe D., Zaritsky D., Markevitch M., Jones C., 2009, ApJ, 691, 963
Clowe D., Bradač M., Gonzalez A. H., Markevitch M., Randall S. W., Jones C., Zaritsky D., 2006, ApJ, 648, L109
Dennison B., 1980, ApJ, 239, L93
Donnert J., Dolag K., Brunetti G., Cassano R., 2013, MNRAS, 429, 3564
Ensslin T. A., Biermann P. L., Klein U., Kohle S., 1998, A&A, 332, 395
Feretti L., Fusco-Femiano R., Giovannini G., Govoni F., 2001, A&A, 373, 106
Feretti L., Brunetti G., Giovannini G., Kassim N., Orrú E., Setti G., 2004, J. Korean Astron. Soc., 37, 315
Feretti L., Giovannini G., Govoni F., Murgia M., 2012, A&AR, 20, 54
Ferrari C., Govoni F., Schindler S., Bykov A. M., Rephaeli Y., 2008, Space Sci. Rev., 134, 93
Giacintucci S. et al., 2005, A&A, 440, 867
Giacintucci S. et al., 2008, A&A, 486, 347
Giovannini G., Feretti L., Venturi T., Kim K.-T., Kronberg P. P., 1993, ApJ, 406, 399
Giovannini G., Bonafede A., Feretti L., Govoni F., Murgia M., Ferrari F., Monti G., 2009, A&A, 507, 1257
Govoni F., Enßlin T. A., Feretti L., Giovannini G., 2001, A&A, 369, 441
Govoni F., Murgia M., Feretti L., Giovannini G., Dallacasa D., Taylor G. B., 2005, A&A, 430, L5
Govoni F., Murgia M., Xu H., Li H., Norman M. L., Feretti L., Giovannini G., Vacca V., 2013, A&A, 554, A102
Heald G., Braun R., Edmonds R., 2009, A&A, 503, 409
Kang H., Jones T. W., 2007, Astropart. Phys., 28, 232
Kang H., Ryu D., Jones T. W., 2012, ApJ, 756, 97
Kempner J. C., Blanton E. L., Clarke T. E., Enßlin T. A., Johnston-Hollitt M., Rudnick L., 2004, in Reiprich T., Kempner J., Soker N., eds, The Riddle of Cooling Flows in Galaxies and Clusters of Galaxies. p. 335, available at: http://www.astro.virginia.edu/coolßow/
Liang H., Hunstead R. W., Birkinshaw M., Andreani P., 2000, ApJ, 544, 686
Liang H., Ekers R. D., Hunstead R. W., Falco E. E., Shaver P., 2001, MNRAS, 328, L21

Macario G., Markevitch M., Giacintucci S., Brunetti G., Venturi T., Murray S. S., 2011, ApJ, 728, 82
Markevitch M., 2006, in Wilson A., ed., ESA Special Publication, Vol. 604, The X-Ray Universe 2005. ESA, Noordwijk, p. 723
Markevitch M., 2012, in Damous T., Jantzen R. T., Ruffini R., eds, Twelfth Marcel Grossmann Meeting on General Relativity, Intergalactic Shock Fronts. World Scientific Press, Singapore, p. 397
O'Sullivan S. P. et al., 2012, MNRAS, 421, 3300
Offringa A. R., de Bruyn A. G., Biehl M., Zaroubi S., Bernardi G., Pandey V. N., 2010, MNRAS, 405, 155
Ogrean G. A., Brüggen M., 2013, MNRAS, 433, 1701
Ogrean G. A., Brüggen M., van Weeren R. J., Röttgering H., Croston J. H., Hoeft M., 2013, MNRAS, 433, 812
Oppermann N. et al., 2012, A&A, 542, A93
Owers M. S., Nulsen P. E. J., Couch W. J., Markevitch M., 2009, ApJ, 704, 1349
Petrosian V., 2001, ApJ, 557, 560
Pizzo R. F., de Bruyn A. G., Bernardi G., Brentjens M. A., 2011, A&A, 525, A104
Rau U., Cornwell T. J., 2011, A&A, 532, A71
Reynolds J. E., 1994, A Revised Flux Scale for the AT Compact Array, AT Memo 39.3/040, available at: http://www.atnf.csiro.au/observers/memos/
Riquelme M. A., Spitkovsky A., 2011, ApJ, 733, 63
Sault R. J., Teuben P. J., Wright M. C. H., 1995, in Shaw R. A., Payne H. E., Hayes J. J. E., eds, ASP Conf. Ser. Vol. 77, Astronomical Data Analysis Software and Systems IV. Astron. Soc. Pac., San Francisco, p. 433
van Weeren R. J., Röttgering H. J. A., Brüggen M., Hoeft M., 2010, Science, 330, 347
Venturi T., Giacintucci S., Dallacasa D., Cassano R., Brunetti G., Macario G., Athreya R., 2013, A&A, 551, A24
Wilson W. E. et al., 2011, MNRAS, 416, 832

This paper has been typeset from a TEX/LATEX file prepared by the author.